Structure of the Calvin-Benson-Bassham sedoheptulose-1,7-bisphosphatase from the model microalga *Chlamydomonas reinhardtii*

Théo Le Moigne[1,2], Martina Santoni[1,3], Lucile Jomat[1], Stéphane D. Lemaire[1], Mirko Zaffagnini[3], Nicolas Chéron[4], Julien Henri[1,*]

1. Sorbonne Université, CNRS, Laboratoire de Biologie Computationnelle et Quantitative UMR 7238, Institut de Biologie Paris-Seine, 4 Place Jussieu, Paris F-75005, France

2. Faculty of Sciences, Doctoral School of Plant Sciences, Université Paris-Saclay, Saint-Aubin F-91190, France

3. Department of Pharmacy and Biotechnology, University of Bologna, Via Irnerio 42, Bologna I-40126, Italy

4. PASTEUR, Département de chimie, École Normale Supérieure (ENS), PSL University, Sorbonne Université, CNRS UMR8640, 75005 Paris, France

*corresponding author

e-mail: julien.henri@sorbonne-universite.fr

Phone: +33144276606

ORCID: Théo Le Moigne 0000-0003-2313-3052; Stéphane Lemaire 0000-0001-6442-0547, Mirko Zaffagnini 0000-0001-5115-0859, Nicolas Chéron 0000-0002-4090-5897; Julien Henri 0000-0003-0772-8881

Abstract

The Calvin-Benson-Bassham cycle (CBBC) performs carbon fixation in photosynthetic organisms. Among the eleven enzymes that participate in the pathway, sedoheptulose-1,7-bisphosphatase (SBPase) is expressed in photo-autotrophs and catalyzes the hydrolysis of sedoheptulose-1,7-bisphosphate (SBP) to sedoheptulose-7-phosphate (S7P). SBPase, along with nine other enzymes in the CBBC, contributes to the regeneration of ribulose-1,5-bisphosphate, the carbon-fixing co-substrate used by ribulose-1,5-bisphosphate carboxylase/oxygenase (Rubisco). The metabolic role of SBPase is restricted to the CBBC, and a recent study revealed that the three-dimensional structure of SBPase from the moss *Physcomitrium patens* was found to be similar to that of fructose-1,6-bisphosphatase (FBPase), an enzyme involved in both CBBC and neoglucogenesis. In this study we report the first structure of an SBPase from a chlorophyte, the model unicellular green microalga *Chlamydomonas reinhardtii*. By combining experimental and computational structural analyses, we describe the topology, conformations and quaternary structure of *Chlamydomonas reinhardtii* SBPase (*Cr*SBPase). We identify active site residues and locate sites of redox- and phospho-post-translational modifications that contribute to enzymatic functions. Finally, we observe that *Cr*SBPase adopts distinct oligomeric states that may dynamically contribute to the control of its activity.

Introduction

Photosynthetic carbon fixation is performed by eleven enzymes that collectively operate the Calvin-Benson-Bassham cycle (CBBC) (Calvin 1962, Johnson 2016), wherein Rubisco plays the prominent role in catalyzing fixation of inorganic carbon onto a pentose acceptor: ribulose-1,5-bisphosphate (RuBP). The net gain of the CBBC is one triose in the form of glyceraldehyde-3-phosphate (G3P) for every three carboxylation reactions catalyzed by Rubisco (Johnson and Alric 2013). Regeneration of RuBP is ensured by the other ten enzymes of the CBBC, among which phosphoribulokinase (PRK) and sedoheptulose-1,7-bisphosphatase (SBPase) are the only enzymes that are exclusively involved in this pathway. The remaining eight enzymes are paralogs of those involved in cytoplasmic glycolysis,

50 gluconeogenesis or the pentose-phosphate pathway. Hence, Rubisco, PRK, and SBPase are expressed
51 in photosynthetic organisms and fulfill biochemical functions so far uniquely attributed to the
52 photosynthetic carbon fixation.
53 Pioneering studies on SBPase were carried out using the native enzyme purified from wheat
54 chloroplasts (Woodrow 1982) and corn leaves (Nishizawa and Buchanan 1981), allowing quantitative
55 assays of its catalytic function. This enzyme catalyzes the hydrolysis of sedoheptulose-1,7-
56 bisphosphate (SBP) into sedoheptulose-7-phosphate (S7P) and requires magnesium ions for both
57 catalysis and activation. In addition, SBPase activity is modulated by pH and redox switching
58 mechanisms (Anderson 1974, Woodrow and Walker 1980, Cadet and Meunier 1988). Redox control
59 is exerted through dithiol/disulfide interchanges dependent upon the ferredoxin-thioredoxin cascade
60 arising from the activity of the illuminated photosystems (Schürmann and Buchanan 1975). In
61 tobacco leaf extracts, SBPase reaches its maximal activity after 10 minutes illumination (Zimmer,
62 Swart et al. 2021), and this activation kinetics is consistent with the slow reduction pattern of
63 *Arabidopsis* SBPase *in vitro* (Yoshida and Hisabori 2018).
64 The crystal structure of SBPase from the moss *Physcomitrium patens* (*Pp*SBPase) has been solved at a
65 resolution of 1.3 Å (Protein Data Bank entry : 5iz3) (Gutle, Roret et al. 2016). *Pp*SBPase fold is highly
66 similar to that of moss fructose-1,6-bisphosphatase (FBPase), yet the protein was shown to
67 distinctively oligomerize as a homodimer and to form a disulfide bridge in a different motif than that
68 found in plant FBPase (Chiadmi, Navaza et al. 1999) (Gütle, Roret et al. 2016). In spite of their
69 homology, the sequences of FBPase and SBPase seem to have evolved different regulatory and
70 catalytic properties that allow different contributions to the CBBC. Indeed, both enzymes specifically
71 recognize their respective 6-carbon and 7-carbon sugar substrates (*i.e.*, fructose-1,6-bisphosphate
72 and SBP, respectively), with only SBPase capable to hydrolyze the other substrate with a resulting
73 catalysis lower than that measured with SBP (Gütle, Roret et al. 2016). To date, the structural
74 components contributing to active site selectivity (*i.e.*, substrate recognition) can be retrieved from
75 two studies reporting the crystal structure of the dual function fructose-1,6-

76 bisphosphatase/sedoheptulose-1,7-bisphosphatase (F/SBPase) from *Thermosynechococcus*
77 *elongatus* in complex with SBP (Cotton, Kabasakal et al. 2015) and from *Synechocystis* sp. PCC 6803 in
78 complex with FBP (PDB entry 3RPL). Recently, it was proposed that the CBBC can bypass fructose-1,6-
79 bisphosphate (FBP) altogether, by only relying on SBP, glycolysis and the oxidative pentose-
80 phosphate pathway paralogs to regenerate the substrate of Rubisco (Ohta 2022).
81 Several studies have reported that SBPase, along with Rubisco, FBPase, aldolase and transketolase,
82 constitute a metabolic bottleneck for the CBBC ((Raines 2022) and references therein).
83 Overexpression of SBPase was found to effectively enhance photosynthesis and growth in plants
84 (Lefebvre, Lawson et al. 2005, Feng, Han et al. 2007, Feng, Wang et al. 2007, Rosenthal, Locke et al.
85 2011, Simkin, Lopez-Calcagno et al. 2017) and in the green microalga *Chlamydomonas reinhardtii*
86 (Hammel, Sommer et al. 2020), indicating that SBPase can be considered as a limiting factor for the
87 photosynthetic carbon fixation. Based on these evidences, it is plausible to consider that SBPase is a
88 good target to improve the photosynthetic capacity by means of metabolic engineering coupled to
89 synthetic biology (Kubis and Bar-Even 2019), especially in the experimentally convenient multi-omic
90 model alga Chlamydomonas (Mettler, Muhlhaus et al. 2014, Schmollinger, Mühlhaus et al. 2014).
91 In Chlamydomonas, SBPase is encoded by a single nuclear gene (Cre03.g185550), and the protein
92 (Uniprot entry P46284) is addressed to the chloroplast by a 54-residue amino-terminal peptide
93 (Emanuelsson, Brunak et al. 2007, Almagro Armenteros, Salvatore et al. 2019). SBPase abundance in
94 the algal cell was quantified by mass spectrometry as 1.1-1.3 ± 0.3 amol/cell, representing 0.15% of
95 total cell proteins (Hammel, Sommer et al. 2020). In Chlamydomonas protein extracts, SBPase was
96 shown to undergo post-translational modifications by phosphorylation of serines and threonines
97 (Werth, McConnell et al. 2017), and redox modifications of cysteine thiols (Zaffagnini, Bedhomme et
98 al. 2012, Morisse, Zaffagnini et al. 2014, Pérez-Pérez, Mauriès et al. 2017). However, the mechanisms
99 by which post-translational modifications affect the catalytic activity of CrSBPase is still lacking. Here,
100 we describe the crystal structures of *Cr*SBPase in two redox states, examine the catalytic activity of
101 recombinant CrSBPase, and investigate the correlation between the redox state and the

102 oligomerization of the protein. Our results suggest that a redox control over oligomer equilibrium
103 could represent a novel mechanism to regulate enzymatic activities in the CBBC.
104

105 **Material and methods**

106 Chemical reagents were purchased from Merck (Darmstadt, Germany), chromatography material
107 was provided by Cytiva (Vélizy-Villacoublay, France), crystallization solutions and consumable were
108 purchased from Qiagen (Hilden, Germany), Hampton Research (Aliso Viejo, CA USA), and SPT Labtech
109 (Melbourn, UK).
110

111 **Cloning and mutagenesis of *Cr*SBPase expression plasmids**

112 The sequence coding for full-length mature SBPase was amplified by reverse transcriptase
113 polymerase chain reaction (RT-PCR) from *Chlamydomonas reinhardtii* total ribonucleic acids extract
114 and inserted at sites 5'-NdeI and BamHI-3' into expression vector pET3c modified for the fusion of an
115 amino-terminal hexa-histidine tag in the recombinant protein, yielding plasmid pSL-175-His_6-
116 *Cr*SBPase-WT. PCR primers were 5'-TCTCGCCATATGGCCGTTCTGACCCAGGCC-3' (forward, NdeI site
117 underlined) and 5'-CGGGTGGGATCCTTAGGCAGCCACCTTCTC-3' (reverse, BamHI site underlined). The
118 encoded protein encompasses 331 amino acids, with a molar mass of 36,176.7 Da and a theoretical
119 extinction coefficient of 24,722.5 $M^{-1}.cm^{-1}$. Unless otherwise stated, amino acid residues numbering
120 is that of GenBank entry DAA79954.1. Point mutants of cysteines 115 and 120 singly substituted with
121 serines were generated by site-directed PCR mutagenesis with primers listed in supplementary table
122 1, producing plasmids pSL-181-His6-*Cr*SBPase-C115S, and pSL-182-His6-*Cr*SBPase-C120S.
123

124 **Recombinant *Cr*SBPase purification**

125 Plasmids pSL-175, -181, and -182 were used to transform *Escherichia coli* BL21(DE3). The
126 transformants were grown at 37 °C in 2YT supplemented with 150 µg/mL ampicillin. When cultures

127 reached an OD_{600} of ~0.6, T7-dependent *Cr*SBPase overexpression was induced by the addition of
128 isopropyl-β-D-thiogalactopyranoside (IPTG) at 0.2 mM for 3 h.
129 Harvested cell pellets were resuspended in 20 mM Tris pH 7.9, 100 mM NaCl (buffer A) and lyzed by
130 1 sec / 1 sec pulsed sonication for 3 min. The soluble fraction of the lysate was separated by 20 min
131 centrifugation at 20,000 *g* and loaded on 2 mL Ni-NTA resin for His-tag mediated affinity
132 chromatography. The resin was washed in four steps with 25 mL buffer A, 25 mL buffer A
133 supplemented with 10, 20, and 30 mM imidazole, and *Cr*SBPase was eluted in three steps with 10 mL
134 buffer A supplemented with 100, 200, and 300 mM imidazole. Pooled eluates containing *Cr*SBPase
135 were loaded on HiLoad Superdex 200 26/600 size-exclusion chromatography column and eluted in
136 buffer A. Protein purity was assessed by electrophoresis on 12% acrylamide gel under denaturing and
137 reducing conditions (supplementary figure 1). Peak fractions were assembled and concentrated by
138 ultrafiltration on Amicon units of MWCO 30,000 Da cut-off. Final concentrations of purified proteins
139 were in the 1-10 mg/ml range as measured by Nanodrop ND-2000 spectrophotometer using an ε_{280}
140 of 24,722.5 $M^{-1}.cm^{-1}$.
141
142 **Western blot**
143 Polyclonal antibodies were generated by immunization of rabbits with pure recombinant *Cr*SBPase
144 (Genecust, Boynes France). Analyzed fractions were separated by denaturing polyacrylamide
145 electrophoresis and transferred to 0.2 µm nitrocellulose membrane for detection with primary
146 antibody subsequently detected by secondary anti-rabbit antibodies coupled to horseradish
147 peroxidase. Detection was done with commercial ECL peroxidase assay (GE Healthcare, Chicago IL
148 USA) with a Chemidoc (Bio-Rad, Hercules CA USA).
149
150 **Crystallization and structure determination**
151 Pure recombinant His6-*Cr*SBPase-WT concentrated at 3-6 mg/mL was tested for crystallization on
152 screens JCSG I-IV in 200 nL sitting drops. Single crystals were obtained and optimized with mother

153 liquor 0.1 M sodium HEPES pH=7.5, 2% (v/v) polyethylene glycol 400, 2.0 M ammonium sulfate, flash-
154 frozen in mother liquor supplemented with 25% glycerol and tested for X-ray diffraction. Complete X-
155 ray diffraction datasets were collected at SOLEIL beamline Proxima-2A and allowed the
156 determination of the crystal structure by model replacement with 5iz3, the structure of ortholog
157 SBPase from the moss *Physcomitrium patens.* Model building in COOT and refinement in the PHENIX
158 software suite yielded structure deposited under PDB ID 7b2o (Emsley, Lohkamp et al. 2010) (Adams,
159 Afonine et al. 2011) (Liebschner, Afonine et al. 2019). After we obtained our experimental structure,
160 the European Bioinformatics Institute (Hinxton, UK) communicated high-accuracy prediction models
161 computed by Deepmind ALPHAFOLD2 (Jumper, Evans et al. 2021), including a prediction of *Cr*SBPase
162 structure (https://alphafold.ebi.ac.uk/entry/P46284) that matches chain A in 7b2o crystal structure
163 with a root mean square deviation (RMSD) of 0.453 Å. Hence, X-ray crystallography and AlphaFold
164 independently contribute to the proposed structural analysis.
165 In order to obtain the structure of *Cr*SBPase in a reduced state, crystals were grown in the presence
166 of 10 mM of the reducing agent tris-(2-carboxyethyl)phosphine (TCEP) in condition JCSG IV E8/56 0.2
167 M lithium sulfate, 0.1 M Tris pH 7.0, and 1.0 M sodium/potassium tartrate. Crystals were cryo-
168 protected in mother liquor supplemented with 25% ethylene glycol, flash-frozen and tested for X-ray
169 diffraction at SOLEIL beamline Proxima-2A. A complete dataset was collected that allowed the
170 determination of the structure by molecular replacement with 7b2o as a template, resulting in
171 structure 7zuv. Among the eight *Cr*SBPase copies of the asymmetric unit, two had their disulfides
172 absent as a consequence of the TCEP treatment while the others six subunits were essentially
173 identical to untreated structures in entry 7b2o (*i.e.*, fully oxidized form).
174
175 **Enzymatic assays**
176 The catalytic activity of 10-200 nM pure recombinant *Cr*SBPase was spectrophotometrically assayed
177 in buffer A by coupling the hydrolysis of 1 mM FBP into F6P to the reduction of 0.5 mM $NADP^+$ into
178 NADPH through isomerization of F6P into glucose-6-phosphate (G6P) by 0.5 $U.mL^{-1}$ phosphoglucose

179 isomerase (PGI) and the oxidation of G6P into 6-phosphogluconolactone (6PGL) by 0.1-0.5 $U.mL^{-1}$
180 glucose-6-phosphate dehydrogenase (G6PDH). Reporter assay is coupled in a molar ratio
181 FBP:F6P:G6P:6PGL of 1:1:1:1 to the oxidation of one molar equivalent of $NADP^+$ into NADPH that we
182 recorded over 20 minutes by measuring the absorbance at 340 nm using a UVIKON
183 spectrophotometer. Pre-treatments with 0-100 mM reduced dithiothreitol (DTTred), 0-30 mM
184 $MgSO_4$, and 0-15 µM recombinant *Cr*TRX-f2 supplemented with 1 mM DTTred (Lemaire, Tedesco et
185 al. 2018) were carried out for 30 min at room temperature before measuring enzyme activity as
186 described above.
187
188 **Titration of accessible cysteine thiols**
189 Quantification of free reactive cysteines on recombinant CrSBPase was performed with 5,5′-dithio-
190 bis-(2-nitrobenzoic acid) (DTNB, Ellman's reagent) mixed with the purified recombinant protein in a
191 200:1 molar ratio in a 1 mL reaction volume containing 100 mM Tris-HCl, pH 7.9 as described
192 previously (Meloni, Fanti et al. 2024). Reaction of DTNB with solvent-exposed cysteine thiols
193 produces 2-nitro-5-thiobenzoate (TNB^-) that we quantified by monitoring the absorbance at 412 nm
194 and a molar extinction coefficient of TNB^- of 14.15 $mM^{-1}.cm^{-1}$. We calculated the number of free
195 reactive cysteines per *Cr*SBPase monomer by dividing the molar concentration of TNB^- by that of the
196 protein.
197
198 **Molecular dynamics**
199 Molecular dynamics (MD) simulations were performed with the Gromacs package (v2021.4). A dimer
200 of CrSBPase was solvated in a rhombic dodecahedron box with at least 8 Å between the protein
201 atoms and the box edges, which corresponds to ~64000 atoms in total (~18000 water molecules) and
202 a triclinic box of 97x97x68 $Å^3$. The box was neutralized with 18 sodium atoms to make it neutral. The
203 starting conformation was the crystallized structure of oxidized CrSBPase, and we protonated C115
204 and C120 to manually create the reduced state. The protein was described with the Amber14SB force

205 field and water with the TIP3P model. Non-bonding interactions were described with standard
206 parameters: van der Waals interactions had a cut-off of 8 Å, and electrostatic interactions were
207 computed with PME with default parameters with a separation between spaces at 8 Å. Bonds
208 containing a hydrogen atom were restrained with the LINCS algorithm with default parameters. After
209 an energy minimization, the system was equilibrated under the NPT conditions with a δt=1 fs
210 timestep, the velocity-rescale thermostat and the Berendsen barostat. Velocities were generated at
211 100 K and the system was heated up to 300 K in 400 ps before performing 100 ps at 300 K. We then
212 ran simulations of 20 µs under the NPT conditions with a δt=2 fs timestep, the velocity-rescale
213 thermostat and the Parrinello-Rahman barostat.
214
215 **Cultivation of Chlamydomonas for native SBPase analysis**
216 *Chlamydomonas reinhardtii* strain D66 was grown in 50 mL Tris-acetate-phosphate (TAP) medium
217 under 40 $\mu E.m^{-2}.s^{-1}$ continuous light until density reached $5x10^4$ $cell.mL^{-1}$, harvested by 10 min
218 centrifugation at 3,000 g. Cell pellet was resuspended in 100 mM Tris-HCl, pH 7.9, 100 mM NaCl, 5
219 mM L-cystéine, 500 µM NADH, and 1 mM EDTA (buffer L) and lysed by 3 freeze-thaw cycles in liquid
220 nitrogen and water bath. Soluble fraction was separated by 10 min centrifugation at 30,000 *g* and
221 loaded for size-exclusion chromatography on a calibrated Superose 6 16/600 column equilibrated in
222 buffer L. Aliquots of 500 µL elution fractions were analyzed by western blot with primary antibodies
223 raised in rabbits against pure recombinant *Cr*SBPase (Covalab, Bron, France) and secondary anti-
224 rabbit IgG coupled to peroxidase (Sigma-Aldrich reference A9169, Saint Louis, USA) revealed by ECL
225 Prime (GE Healthcare).
226
227 **Small-angle X-ray scattering**
228 Pure recombinant *Cr*SBPase was injected on Agilent HPLC BioSEC-3 300 column in buffer A, in line
229 with the X-ray beam capillary at SOLEIL beamline SWING. *Cr*SBPase was untreated or pre-treated

230 with 10 mM of reducing agent dithiothreitol (DTTred). Diffusion curves were analyzed with ATSAS
231 software to determine the molecular mass and oligomeric state of the protein.
232

233 **Results and Discussion**

234 **Crystal structure of *Cr*SBPase**

235 Pure recombinant *Cr*SBPase crystallized in space group $P2_12_12$ and provided a complete X-ray
236 diffraction dataset at a resolution of 3.09 Å. The asymmetric unit is composed of six polypeptide
237 chains packing as three dimers and four water molecules could be modeled. All chains align within a
238 root mean square deviation (RMSD) <0.25 Å and can be considered identical. 309 out of the 331
239 residues were built in the electron density, the unmodelled sequences are in the disordered
240 extensions at the amino- and carboxy-termini of the model. *Cr*SBPase folds into two distinct domains
241 (figure 1A-B). The amino-terminal domain (NTD, residues 73-247) is composed of helices 1, 2, and 3
242 and a mixed β-sheet formed by strands 3-9. The carboxy-terminal domain (CTD, residues 248-383) is
243 composed of helices 4, 5, and 8 and helices 6 and 7 that sandwich a mixed β-sheet formed by strands
244 10-13. α-helices 1-3 pack on the amino-terminal end of the seven-strand sheet, while α-helices 4,5,
245 and 8 pack on the carboxy-terminal end of the four-strand sheet. α-helices 6 and 7 are sandwiched in
246 between the two sheets. *Cr*SBPase chain A aligns with previously reported crystal structure of
247 *Pp*SBPase with an RMSD of 0.478 Å (Gütle et al. 2018 PDB 5IZ3). This close structural similarity
248 between orthologues indicates common structural properties supporting a conservation of the
249 SBPase function in the evolutionary time separating the microalga Chlamydomonas from the land
250 moss *P. patens*. A short antiparallel β-sheet is constituted of 4-residue strands 1 and 2 separated by a
251 β-turn and preceded by loop A_{113}SCAGTAC_{120}. This motif projects to solvent from α-helices 2 and 3
252 (figure 1C-D). Residues 113-130 forming the loop and β-hairpin (LBH) motif are positioned away from
253 the core of the protein, at 15.3 Å from water molecule 401 (W401), and will be further discussed in
254 the next sections.

255 AF2 entry AF-P46284-F1-model_v4 from AlphaFold Protein Structure Database aligns with our crystal
256 structure 7b2o chain E with RMSD = 0.434 Å, showing excellent agreement between experiment and
257 prediction at the level of protein main chain. Exceptions are in local differences in several loops
258 conformations and in the N-ter and C-ter borders of secondary structure elements. Numerous amino
259 acid residues side chains adopt moderately distinct orientations between the computational model
260 and the experimental structure.
261 AF3 was recently communicated (Abramson, Adler et al. 2024) along with its online prediction server
262 hosted at https://golgi.sandbox.google.com/. *Cr*SBPase model from AF3 align to our crystal structure
263 7B2O chain A with RMSD = 0.489 Å showing again their strong similarity and with a small discrepancy
264 between AF2 and AF3 models with RMSD = 0.216 Å. The only significant deviations between 7B2O
265 and AF3 are in the orientation of several side chains and notably on the conformation of region 114-
266 131 that contain the LBH motif.
267
268 **CrSBPase catalytic pocket**
269 *Cr*SBPase is structurally similar to its ortholog from the moss *Physcomitrium patens* (RMSD=0.478 Å)
270 (Gutle, Roret et al. 2016). SBPase is a homolog of FBPase, another enzyme involved in the CBBC in
271 photosynthetic organisms and also ubiquitously involved in neoglucogenesis. Cytosolic isoforms of
272 FBPase from non-plant sources have been extensively studied (Moorhead, Hodgson et al. 1994, Lee
273 and Hahn 2003). For instance, the crystal structure of human muscle FBPase complexed with its
274 substrate (FBP) was solved (PDB entry: 5l0a, to be published). We aligned the structure *Cr*SBPase
275 onto this human FBPase:FBP complex from entry 5l0a, confirming their similarity (RMSD = 0.824 Å)
276 with the notable exception of the LBH motif which is absent in FBPase. In a 4-Å distance to FBPase
277 co-crystallized with FBP we aligned 12 residues that are likely available for FBP or SBP binding by
278 *Cr*SBPase (figure 1E): E155, D173, D176, G177, Y287, G289, G290, M291, K317, L318, R319, and E323.
279 These residues are exposed to the solvent in a continuous surface (figure 1F). W401 could be
280 modelled at the center of the putative SBPase catalytic pocket, in the vicinity of E155, D173, D176,

281 R319, and E323, in the catalytic pocket predicted from alignment with human FBPase bound to FBP.
282 W401 specifically is in bonding distance to catalytic residues D178, D181, and E328. W401 is likely to
283 hydrolyze the substrate SBP.
284
285 **Sites of redox post-translational modifications**
286 Ten cysteines could be located in each monomer of *Cr*SBPase (C115, C120, C149, C153, C169, C222,
287 C231, C340, C355, C362). Previous redox-based proteomic studies exploiting Chlamydomonas cells or
288 protein extract established that *Cr*SBPase undergoes redox modifications by thioredoxin-dependent
289 dithiol/disulfide exchange (Lemaire, Guillon et al. 2004, Pérez-Pérez, Mauriès et al. 2017),S-
290 glutathionylation (Zaffagnini, Bedhomme et al. 2012), or S-nitrosylation (Morisse, Zaffagnini et al.
291 2014). While the putative Cys sites for S-glutathionylation are not known, thioredoxin and S-
292 nitrosylation Cys targets were identified as being C222/C231/C355/C362, and C355/C362,
293 respectively. DTNB-based thiol titration on the native purified SBPase indicates that 4.0 ± 0.6
294 cysteines are likely reactive owing to their relative exposure to solvent in a free thiol form. Amino
295 acid residue accessible surface area and accessibility (ASA) calculation is consistent with DTNB
296 titration, with C149, C153, C231, and C355 exposed to the solvent (ASA respective areas: 0.154 Å^2,
297 0.113 Å^2, 0.308 Å^2, and 10.083 Å^2), and the six others either shielded from solvent (C169, C222, C340,
298 and C362) or engaged in a disulfide bridge (C115, C120) (Ahmad, Gromiha et al. 2004). In *Cr*SBPase
299 crystal structure, C222 and C231 are positioned on neighboring strands of the amino-terminal
300 domain, exposing their thiol 3.5 Å away from each other (figure 1G, supplementary figures 2A-B). The
301 formation of an intramolecular disulfide bridge at this cysteines pair is possible if local main chain
302 rearrangements allow a closer contact. C362 thiol is positioned 10.5 Å away from the nearest thiol
303 group of C340. Additionally, C340 and C362 are exposed on an opposite side of the carboxy-terminal
304 β-sheet, disfavoring the formation of an internal disulfide bridge. C355 points its side chain towards
305 C153 and C169 with a thiol-thiol distance of 4.6 Å and 10.1 Å, respectively. Although not observed in
306 our model, a C355-C153/C169 dithiol-disulfide exchange is thus plausible, as described for plant

307 FBPase (Jacquot, Lopez-Jaramillo et al. 1997). Local rearrangements that occur upon FBPase disulfide
308 reduction causes a larger scale relaxation of the active site required to reach maximal catalytic
309 potential (Chiadmi, Navaza et al. 1999) as kinetically characterized for enzymes from *Arabidopsis*
310 *thaliana* (Yoshida and Hisabori 2018) and *Nicotiana benthamiana* (Zimmer, Swart et al. 2021). In
311 Chlamydomonas and Physcomitrium SBPases, the FBPase-type regulatory disulfide is not observed
312 but the SBPase-type C115-C120 bridge is conserved in a nearly identical position in the LBH motif
313 where it may regulate the enzyme by alternative conformational rearrangements. Indeed, the
314 disulfide-bonded cysteines constrain Chlamydomonas SBPase loop A_{113}SCAGTAC_{120} into a compact
315 lasso that could open into a relaxed conformation hypothetically activating catalysis.
316

317 **Sites of post-translational phosphorylations**

318 *Cr*SBPase was reported to be phosphorylated from algae extracts at residues T112, S114, T118, S123,
319 T310, S311, and T313 (Wagner, Gessner et al. 2006, Werth, McConnell et al. 2017, McConnell, Werth
320 et al. 2018). Consistently with the proximity of these residues in two sectors of the sequence
321 (supplementary figure 3), the candidate modification sites are located in two contiguous regions in
322 the three-dimensional structure (figure 1H). T112, S114, T118, and S123 are exposed to the solvent
323 of the amino-terminal domain. The residues belong to or are located nearby the A_{113}SCAGTAC_{120}
324 motif where phosphorylations may cross-signal with redox modifications on C115 and C120. T310,
325 S311, and T313 are located on the other edge of the enzyme, at the solvent exposed tip of the
326 carboxy-terminal domain. Their co-localization at the T_{310}SPT_{313} motif likely facilitates a coordinated
327 phosphorylation of the three residues by the same kinase. Because both groups of potential
328 phospho-sites are located at 17-18 Å from the catalytic pocket (W401 taken as a reference point),
329 there is no straightforward mechanism by which such modifications would exert a control over
330 *Cr*SBPase activity. Analysis of phospho-mimicking mutants along with the identification of the actual
331 kinases/phosphatases couples that control *Cr*SBPase phosphorylation state would allow to
332 comprehend the role of this putative regulatory mechanism.

333

334 ***Cr*SBPase enzymatic activity**

335 Recombinant *Cr*SBPase was assayed for its capacity to catalyze FBP hydrolysis into F6P (Gutle, Roret
336 et al. 2016), a proxy for the hydrolysis of SBP into S7P that we could not test by lack of available
337 substrate and kinetic reporter method. Previous studies demonstrated that plant SBPase requires the
338 cofactor Mg^{2+} and a chemical reductant (DTTred) to be fully activated *in vitro*, reaching a K_M value of
339 0.05 mM and a k_{cat} of 81 sec^{-1} in optimal conditions (Anderson 1974, Woodrow and Walker 1980,
340 Cadet and Meunier 1988). In agreement with this, we found a total absence of activity in the
341 untreated *Cr*SBPase (data not shown), whereas pre-incubation of the enzyme with DTTred and Mg^{2+}
342 resulted in a strong activation (figure 2). By testing different concentrations of $MgSO_4$ (3, 10, 15, and
343 20 mM) and DTTred (1, 10, 25, 50, and 100 mM), we established that 10 mM of DTT and 10 mM
344 $MgSO_4$ are the optimal conditions to attain the maximum specific activity (figure 2A and 2B).
345 Unexpectedly, DTTred concentrations above 10 mM had an inhibitory effect, causing a drastic drop in
346 activity that probably resulted from structural effects leading to denaturation of the enzyme (figure
347 2A). In contrast, we observed no such inhibitory effect in the presence of magnesium at
348 concentrations above 10 mM (figure 2B). Under physiological conditions, the light-dependent redox
349 regulation of plant SBPase is specifically exerted by f-class thioredoxins (Gutle, Roret et al. 2016),
350 which are reduced by the ferredoxin-thioredoxin cascade (Schürmann and Buchanan 1975). The
351 chloroplast TRX-f2 from *Chlamydomonas reinhardtii* was thus tested and validated for its capacity to
352 activate *Cr*SBPase by reduction (figure 2C). The maximum activity, corresponding to 12.15 ± 2.15
353 µmol(NADPH) min^{-1} mg(SBPase)$^{-1}$, was obtained by pre-incubating the enzyme with 1 µM *Cr*TRX-f2
354 supplemented with 1 mM DTT and 10 mM $MgSO_4$, and maintained even at higher *Cr*TRX-f2
355 concentrations (*i.e.*, 5 and 10 µM) (figure 2C). *Cr*SBPase specific activity that we report is comparable
356 to that reported for spinach SBPase with FBP as substrate (3.5 µmol min^{-1} mg^{-1} (Seuter, Busch et al.
357 2002)) and to that reported for another recombinant Chlamydomonas SBPase with SBP as substrate
358 (7.15 ± 0.61 µmol min^{-1} mg^{-1} (Tamoi, Nagaoka et al. 2005)).

359

360 **Redox controlled dynamics of *Cr*SBPase**

361 *Cr*SBPase crystallized under reducing treatment (10 mM TCEP). Among the eight subunits in the
362 asymmetric unit, C115-C120 disulfide is absent in two chains (subunits C colored in magenta and
363 subunits E colored in salmon, figure 3D and 3F), while the other six subunits still have the C115-C120
364 disulfide bridge (figure 3B,C,E,G-I). All other cysteines are unaffected by the reducing treatment,
365 consistently with their thiol form in crystal structure of oxidized state. These six subunits present
366 mildly variable conformations of the A_{113}SCAGTAC_{120} lasso conformation similar to the untreated
367 oxidized structure of *Cr*SBPase (figure 3A). Reduction of the C115-C120 disulfide increases local
368 disorder, and the main chain electron density became uninterpretable over a few residues for
369 subunits C (residues 115-118, 124-127), and subunits E (residues 119-127) (supplementary figure 4).
370 Molecular dynamics (MD) simulations of the reduced structure were performed by starting from a
371 dimer of the crystallized oxidized form and forcing C115 and C120 residues to be reduced in the thiol
372 state (-SH). We then ran two independent replicas of 20 µs of MD. In addition, we also ran two
373 independent replicas of 2 µs of MD in the oxidized form. In one of the replicas of the reduced form
374 (MD1), the protein structure barely changed as observed in the SG(C115)/SG(C120) distance that
375 plateaued at ~7 Å, as well as in the RMSD with respect to the starting conformation that stayed
376 around 2 Å (see supplementary figures 8-9 for plots and 12 for images of the structures). However, in
377 the other replica of the reduced form (MD2), significant changes of conformation appeared: the
378 SG(C115)/SG(C120) distance ended up at ~10 Å with peaks at 20 Å and the RMSD values ended up at
379 3.7 and 2.8 Å (supplementary figures 8-9). The difference between MD1 and MD2 is stronger when
380 one focuses on the RMSD of the mobile motif (residues 112 to 131, supplementary figure 10). We
381 observed that after 17 µs of MD all chains adopted an equilibrated conformation and then fluctuated
382 around that conformation (supplementary figure 10); representative structures extracted from MD
383 were thus obtained from a clustering on the time frame (or block) 17-20 µs.

384 The two chains A and B from MD2 adopt a different final conformation (see figure 4A for the overlap
385 with the crystallized oxidized structure and figure 4B for the overlap with the crystallized reduced
386 structure), and we cannot directly conclude on which one is the most stable. Moreover, the residues
387 115 to 128 of each chain from MD1/2 do not overlap well with the crystallized reduced structure
388 which means that neither of the two chains conformations from MD simulations has converged
389 towards the crystallized state. However, we can observe in the reduced crystallized structure that
390 residues 134-148 form an α-helix which is also present in chain B from MD2 whereas this structure is
391 not kept in chain A from MD2 (see green chain on the right of figures 4A-B). In addition, mobile motif
392 from chain B seems to open towards the solvent in a similar way with what was observed for FBPase
393 (Chiadmi, Navaza et al. 1999). Thus, we conclude that chain B from MD2 is more representative of
394 the true reduced conformation than chain A from MD2. If we compare the mobility of chain B from
395 MD2 in the reduced state with one chain in the oxidized state (also chain B from MD2), we can see
396 that the mobile motif is overall more flexible in the reduced state, which is especially true for
397 residues around C120 (residues 118 to 123, supplementary figure 11). We then analyzed the RMSD
398 of residues 112 to 131 from chain B during MD2 (supplementary figure 12): residues 112, 130 and
399 131 barely move which is expected since they belong or are directly connected to the two α-helixes
400 flanking the mobile motif. At ~6 µs of the trajectory almost all other residues (113-129 residues with
401 the sole exception of C120) display an abrupt change of conformation, with a different magnitude
402 though: starting from ~2 Å, the RMSD jumped to 3 Å for some residues (residue 129) and to 15 Å for
403 other residues (residues 125, 126) (supplementary figures 9, 10, and 12). At ~13.5 µs, another
404 change occurs which involves C120 but not all the other residues. Thus, we conclude that the
405 opening of the mobile motif happens in a concerted way and not sequentially residue per residue.
406
407 **Oligomeric states of *Cr*SBPase**
408 Previous studies reported a homodimeric state for SBPase from the moss *Physcomitrella patens*,
409 deduced from the quaternary structure of recombinant protein in the asymmetric unit of the crystal

410 (Gütle, Roret et al. 2016). Size-exclusion chromatography (SEC) profile of *Cr*SBPase is polydisperse
411 with at least three distinct oligomeric states (figure 6A). Notably, we observed that the protein elutes
412 as a main peak of 79 kDa, close to the mass of a homodimer (theoretical mass from monomer
413 sequence: 36,176.7 Da) and consistently with the crystallized state of moss enzyme. Thorough
414 inspection of the elution profile of *Cr*SBPase revealed a peak broadened by a later-eluting shoulder,
415 with the apparent molecular mass of the tailing species at 48 kDa suggesting the presence of a
416 monomeric state of *Cr*SBPase *in vitro*. A third *Cr*SBPase species elutes at an apparent molecular mass
417 of 145 kDa, that fits with a homotetramer. According to the absorbance of each peak and considering
418 that they represent all states of purified and oxidized *Cr*SBPase in solution, we estimate a repartition
419 percentage of species of 10:53:37 for the tetramer:dimer:monomer mixture (total = 100%). Re-
420 injection of the dimer peak fraction over size-exclusion chromatography yielded a similar mixed
421 profile, supporting a dynamic equilibrium over the time of the experiment (>2 h) (data not shown).
422 *Cr*SBPase was crystallized in space groups $P2_12_12$ or $P12_11$ with respectively 6 and 8 protomers in the
423 asymmetric unit. Proteins Interfaces Structures and Assemblies (PISA) analysis reveals that
424 protomers of both crystals pack as homodimers with extensive subunit interface of buried area 4,170
425 $Å^2$ in a similar manner (figure 5A) (Krissinel and Henrick 2007). In the asymmetric unit of *Cr*SBPase
426 crystallized in reducing conditions (7zuv) or within crystallographic neighboring units of *Cr*SBPase in
427 oxidized state (7b2o), *Cr*SBPase further packs into a homotetramer, a dimer of dimers (figure 5B).
428 The apparent molecular mass of SBPase extracted from *Chlamydomonas* cultures cultivated in TAP
429 medium under 40 $\mu E.m^{-2}.s^{-1}$ illumination is comprised between 130 and 40 kDa with the homodimer
430 representing the predominant state as supported by immunoblot analysis (figure 6B).
431 To further investigate the oligomeric dynamics of CrSBPase, we performed small-angle X-ray
432 scattering (SAXS) analysis of purified (untreated) or reduced enzyme *in vitro* which reveals an
433 increase in the protein radius of gyration from 39 to 62 Å upon reduction (supplementary figure 6).
434 This observation implies a change in the oligomeric state of *Cr*SBPase correlating with the redox
435 state. As a matter of fact, purified *Cr*SBPase tends to precipitate into amorphous aggregates that can

436 be turned into droplets of liquid-liquid phase separation by treatment with 10 mM TCEP
437 (supplementary figure 7). Since the LBH redox module is positioned at the homodimer interface
438 (figure 5C), we postulated that the reduction of the C115-C120 disulfide bond and the subsequent
439 local conformation changes depicted by MD affect the oligomer equilibrium of the enzyme. As a
440 matter of fact, we observed that protein mutants C115S or C120S, which are unable to form the
441 C115-C120 disulfide bond, elute in a different oligomer ratio than wild-type CrSBPase (figure 6A).
442 Indeed, we observed a relative accumulation of monomer and tetramer species at the expense of the
443 dimer state in both mutants. This suggests that C115-C120 is involved in the stabilization of the
444 dimer. Meanwhile, the activity of the two Cys mutants still responded to DTT/Mg-dependent
445 activation resembling the response of the wild-type protein. No activity was detected for native and
446 untreated forms, while specific activities of C115S and C120S mutants upon treatment with DTT and
447 $MgSO_4$ (10 mM for both compounds) were respectively 96% and 107% with respect to wild-type
448 maximum activity (13.3 ± 2.5 and 14,9 ± 0,9 µmol(NADPH) min^{-1} mg(SBPase)$^{-1}$ for C115S and C120S
449 mutants, respectively, supplementary figure 14). Based on these data, we can thus conclude that
450 C115-C120 disulfide bond is not the sole thiol-dependent regulatory mechanism involved in the
451 modulation of *Cr*SBPase activity and that the redox dependency of *Cr*SBPase catalysis likely depends
452 on other cysteine pairs. Future studies are required to shed light on the identity of cysteine residues
453 that contribute to *Cr*SBPase catalytic modulation other than C115 and C120.
454

455 **Conclusions and perspectives**

456 We report the first crystal structure of an SBPase from the microalga *Chlamydomonas reinhardtii*, a
457 model for the molecular and cell biology of plants. SBPase is a photosynthetic enzyme involved in the
458 regeneration phase of the CBBC cycle proved to be target of multiple regulations that we map onto
459 our structural model. The native folding of *Cr*SBPase is highly similar to that of SBPase from the moss
460 *Physcomitrium patens* and to FBPase from chloroplast or cytoplasmic origins. Notwithstanding its
461 propensity to form crystals, recombinant *Cr*SBPase encompasses a range of oligomeric states,

462 dominated by a homodimeric form susceptible to exchange for monomers, tetramers and higher-
463 order assemblies. This oligomer equilibrium is dynamic and correlates with the presence of a
464 disulfide bridge at the vicinity of the monomer-monomer interface, in the SBPase-specific LBH motif.
465 We postulate that the reversible reduction/oxidation of the C115-C120 pair modulates the
466 oligomerization of *Cr*SBPase, through the induction of a local disorder that we observed in the crystal
467 structure of the protein under reducing conditions and that correlates with computations of
468 molecular dynamics.
469 How this oligomeric exchange impacts the actual activity of the enzyme is an open question but
470 should be aligned with previous reports on the allosteric character of the structurally similar FBPase
471 enzyme which follows dimer/tetramer exchanges (Barciszewski, Wisniewski et al. 2016) with a Hill
472 cooperativity coefficient close to 2 representing positive cooperativity in the context of a homodimer
473 (Giudici-Orticoni, Buc et al. 1990). Recent *in vivo* proteome mapping in *Chlamydomonas reinhardtii*
474 localized SBPase in a punctate region surrounding the Rubisco pyrenoid nearby five other CBBC
475 enzymes: phosphoglycerate kinase 1 (PGK), glyceraldehyde-3-phosphate dehydrogenases (GAP1,
476 GAP3), fructose-bisphosphate aldolase (FBA3), ribulose-5-phosphate 3-epimerase (RPE1), and
477 phosphoribulokinase (PRK) (Wang, Patena et al. 2022). Based on our structure-function study on
478 recombinant SBPase, we can speculate that the altered redox state of SBPase may influence the
479 movement to or from the liquid partition of the stroma, where SBPase is metabolically required to
480 provide its contribution to CBBC reactions near other enzymes of the pathway.
481

482 **Tables.**

483 Table 1. Crystallographic data collections and models building statistics.

	7b2o (untreated)	7zuv (partially reduced)
Wavelength (Å)	0.9801	0.9801
Resolution range (Å)	46.62 - 3.095 (3.206 - 3.095)	48.54 - 3.11 (3.221 - 3.11)
Space group	P 2_1 2_1 2	P 1 2_1 1
Unit cell (Å, °)	178.224 183.652 75.196 90 90 90	53.774 163.462 172.765 90 91.939 90
Total reflections	615155 (55989)	376091 (32376)
Unique reflections	45740 (4245)	53456 (5213)
Multiplicity	13.4 (12.9)	7.0 (6.2)
Completeness (%)	99.34 (94.20)	99.65 (97.17)
Mean I/sigma(I)	12.02 (1.72)	8.54 (1.30)
Wilson B-factor (Å²)	64.82	68.45
R-merge	0.495 (1.877)	0.2492 (1.502)
R-meas	0.5144 (1.954)	0.2691 (1.64)
R-pim	0.1386 (0.5343)	0.1009 (0.6477)
CC1/2	0.983 (0.623)	0.988 (0.479)
CC*	0.996 (0.876)	0.997 (0.805)
Reflections used in refinement	45607 (4242)	53417 (5193)
Reflections used for R-free	1986 (183)	1983 (191)
R-work	0.1942 (0.3071)	0.1963 (0.3239)
R-free	0.2390 (0.3482)	0.2328 (0.3740)
CC(work)	0.944 (0.788)	0.956 (0.726)
CC(free)	0.912 (0.649)	0.949 (0.596)
Number of non-hydrogen atoms	14194	18714
Macromolecules	14190	18704
Solvent	4	10
Protein residues	1859	2451
RMS(bonds) (Å)	0.005	0.004
RMS(angles) (°)	0.75	0.73
Ramachandran favored (%)	94.26	94.80
Ramachandran allowed (%)	5.52	4.70
Ramachandran outliers (%)	0.22	0.50
Rotamer outliers (%)	0.13	0.55
Clashscore	4.88	6.60
Average B-factor (Å²)	67.00	68.41
macromolecules (Å²)	67.01	68.40
solvent (Å²)	49.59	94.37

484 Statistics for the highest-resolution shell are shown in parentheses.

485

486 **Figures legends**

487 **Figure 1. Crystal structure of *Cr*SBPase.**

488 (**A**) Topology is displayed as cartoon with main chain colored from blue (amino-terminus) to red
489 (carboxy-terminus). (**B**) Rotated view of A. by x-axis over -90°. (**C**) Close-up view of region
490 A_{113}SCAGTAC_{120} with disulfide bond shown in sticks. (**D**) Rotated view of C. by x-axis over -90°. (**E**)
491 Putative active site residues inferred from alignment with FBPase bound to FBP (5l0a, human muscle
492 fructose-1,6-bisphosphatase E69Q mutant in active R-state in complex with fructose-1,6-
493 bisphosphate) are represented in sticks. Residue numbering is according to Chlamydomonas SBPase
494 Uniprot entry P46284. (F) Surface representation in the B. orientation with putative active site
495 residues colored in cyan. Water molecule 401 (W401) oxygen is represented as a red sphere. (G)
496 Cysteines site chains are represented in spheres. (H) Threonines and serines side chains reported to
497 be the target of phosphorylations are represented in spheres.

498

499 **Figure 2. Functional characterization of CrSBPase *in vitro*.**

500 Reported enzymatic activity of *Cr*SBPase assayed for (**A**) reduction by reduced dithiothreitol (DTTred)
501 and 10 mM of $MgSO_4$, (**B**) Magnesium sulfate ($MgSO_4$) and 10 mM DTTred, and (**C**) recombinant
502 thioredoxin f2 from *Chlamydomonas reinhardtii* (*Cr*TRX-f2) and 10 mM $MgSO_4$, 1 mM DTT.

503

504 **Figure 3. Crystallographic structures of *Cr*SBPase under reducing treatment: local disorder of the**
505 **A_{113}SCAGTAC_{120} loop.**

506 Main chain was traced according to crystallographic b-factor, with large orange sections representing
507 high b-factor values and thin blue sections representing low b-factors. A-I. Aligned structures of
508 *Cr*SBPase protomers without redox treatment (A, 7b2o chain A) or in the presence of 10 mM TCEP
509 reducing agent (B-I, 7zuv chains A-H).

510

511

512

513 **Figure 4. Molecular dynamics simulation of *Cr*SBPase after reduction.**

514 (**A**) Overlap of the crystallographic structure of oxidized *Cr*SBPase and representative structures of
515 equilibrated reduced *Cr*SBPase during molecular dynamics simulation 2 (MD2). For structures
516 extracted from MD, only residues 109 to 148 are displayed since most of the other residues are
517 closely overlapping those of the crystallographic structure. (**B**) Overlap of the crystallographic
518 structure of reduced *Cr*SBPase and representative structures of equilibrated reduced *Cr*SBPase
519 during MD2. For structures extracted from MD, only residues 109 to 148 are displayed.

520

521 **Figure 5. Oligomeric state of *Cr*SBPase in the crystal.**

522 (**A**) Asymmetric unit dimer of untreated *Cr*SBPase (7b2o). Chains are represented in cartoon and
523 colored cyan (chain B) and salmon (chain E). (**B**) Asymmetric unit homotetramer under reducing
524 treatment (7zuv). Chains A (cyan), C (magenta), F (white), and H (orange) belong to the same
525 asymmetric unit. (**C**) Close-up view on figure A homodimer interface. Loop 113-ASCAGTAC-120 from
526 chain B (in cyan) is in 5-Å distance of neighboring chain E (in salmon). C115 and C120 are bonded by a
527 disulfide bridge.

528

529 **Figure 6. Oligomeric state of *Cr*SBPase *in vitro*.**

530 (**A**) Size-exclusion chromatograms of *Cr*SBPase wild-type (blue), mutant C115S (orange), mutant
531 C120S (gray) on Superdex 200 26/600 GL column. (**B**) Size-exclusion fractionation of Chlamydomonas
532 cell extracts. Chlamydomonas cell culture was harvested, lysed and the soluble fraction of the lysate
533 was loaded on Superose6 16/600 size-exclusion column. Chromatography fractions were analyzed by
534 western blot with anti-*Cr*SBPase primary antibodies. First membrane was loaded with fractions
535 eluted from 40 to 80 mL. Second membrane was loaded with fractions eluted from 80 to 120 mL. M
536 lane is loaded with molecular mass standards ladder. Recombinant CrSBPase was loaded was loaded
537 on the last lane to the right..

538

539 **Supplementary information**

540 **Supplementary table 1. Primers used for point mutagenesis.**

5'-forward C115S	CCGCACCGCCTCGAGCGCCGGTACCGCCTGCGTG
3'-reverse C115S	CACGCAGGCGGTACCGGCGCTCGAGGCGGTGCGG
5'-forward C120S	GCGCCGGTACCGCCAGCGTGAACAGCTTCGGCG
3'-reverse C120S	CGCCGAAGCTGTTCACGCTGGCGGTACCGGCGC

541

542 **Supplementary figure 1. Purification of recombinant *Cr*SBPase.**

543 A. Size-exclusion chromatography profile recorded at absorbance λ= 280 nm on Superdex 200 26/600
544 GL column. B. Electrophoresis of affinity-chromatography fractions on 12% acrylamide gel in
545 denaturing and reducing condition. Gel was stained with Coomassie blue. Mw: molecular mass
546 standards ladder.

547

548 **Supplementary figure 2. Cysteines pair C222-C231 close-up view.**

549 *Cr*SBPase structure 7b2o zoomed around the pair of cysteines 222 and 231 suggests they may form a
550 reversible disulfide bridge, with a thiol-to-thiol distance of 3.5 Å.

551

552 **Supplementary figure 3. SBPase multiple sequences alignment.**

553 *Cr*SBPase mature sequence was used for a BLAST search. Retrieved homolog sequences were aligned
554 and colored-coded according to residue conservation. Illustration made with EndScript (Robert and
555 Gouet 2014).

556

557 **Supplementary figure 4. Related to figure 3. Crystallographic structures of *Cr*SBPase under reducing**
558 **treatment: local main chain rearrangement and variety of cysteine states of the A_{113}SCAGTAC_{120}**
559 **loop.**
560
561
562 **Supplementary figure 5. Surface representation of 7b2o homodimer, colored according to ConSurf**
563 **(Glaser, Pupko et al. 2003) conservation score from teal (lowest conservation) to purple (highest**
564 **conservation) among 150 aligned homologs.**.
565
566 **Supplementary figure 6. Size-exclusion chromatography coupled to small angle X-rays scattering**
567 **(SEC-SAXS) of *Cr*SBPase.**
568 A. X-ray scattering curve log(I) = f(s) for pure *Cr*SBPase untreated (dark blue) or treated (light blue)
569 with 10 mM reduced dithiothreitol (DTTred). B. Radius of gyration of untreated protein was
570 computed by ATSAS Primus Guinier Wizard as Rg = 39.14 ± 0.06 Å (Franke, Petoukhov et al. 2017). C.
571 Radius of gyration of DTT-treated protein was computed as Rg = 62.47 ± 0.38 Å.
572
573 **Supplementary figure 7. Phase separation of reduced *Cr*SBPase precipitates.**
574 *Cr*SBPase at 2 mg/mL formed amorphous precipitates after storage at 4 °C for a week. The
575 suspension was sedimented by centrifugation at 20,000 *g* for 20 minutes and a microliter drop of the
576 supernatant or of the pellet were treated with 10 mM TCEP and visualized by binocular optical
577 microscope. A. Untreated precipitate. B. TCEP-treated precipitate. C. Untreated supernatant. D.
578 TCEP-treated supernatant.
579
580 **Supplementary figures 8-12. Computational detail of molecular dynamic simulation.**
581

582 **Supplementary figure 8.**

583 SG(Cys115)/SG(Cys120) distances along the MD trajectories for each chain (left: oxidized state, right:
584 reduced state). Light colors: raw data saved every 100 ps, dark colors: moving average on 20ns blocs.

585

586 **Supplementary figure 9.**

587 RMSD of main chain along the MD trajectories for each chain (left: oxidized state, right: reduced
588 state). Light colors: raw data saved every 100 ps, dark colors: moving average on 20 ns blocs.

589

590 **Supplementary figure 10.**

591 RMSD of main chain of the mobile motif in the reduced state (residues 112 to 131) along the MD
592 trajectories for each chain (left: RMSD with respect to the starting conformation of MD, right: RMSD
593 with respect to the conformation at 20 µs). Light colors: raw data saved every 100 ps, dark colors:
594 moving average on 20 ns blocs.

595

596 **Supplementary figure 11.**

597 RMSF per residue for each chain (top row: full sequence, bottom row: zoom on residues 110 to 170;
598 left column: oxidized state, middle column: reduced state, right column: comparison of one chain
599 from each state).

600

601 **Supplementary figure 12.**

602 RMSD of main chain of each residue from the mobile motif along the trajectory of chain B from MD2.
603 Data are moving average on 200 ns blocs.

604

605 **Supplementary figure 13. Structures of *Cr*SBPase retrieved from molecular dynamics simulations 1**
606 **and 2**.
607 Two independent replicas of 20 µs were performed. In one of them (MD1), the overall structure of
608 both chains of the enzyme barely changed. To illustrate this, we present in supplementary figure 12
609 the overlap between the crystallographic oxidized structure and representative structures extracted
610 from MD (based on clustering the last 3 µs since each chain does not display significative changes
611 after 17 µs). A. Overlap of the crystallographic structure of oxidized *Cr*SBPase and representative
612 structures of equilibrated reduced SBPase during MD1. For structures extracted from MD, only
613 residues 111 to 132 are displayed since the other residues are closely overlapping those of the
614 crystallographic structure. B. Overlap of the crystallographic structure of oxidized SBPase and
615 representative structures of equilibrated reduced *Cr*SBPase during MD2. For structures extracted
616 from MD, only residues 109 to 148 are displayed since most of the other residues are closely
617 overlapping those of the crystallographic structure.
618
619 **Supplementary figure 14.** Regulatory properties of CrSBPase activity.
620 Specific activities of wild-type form (wt) and cysteine mutants (C115S and C120S) were evaluated by
621 treating each *Cr*SBPase form without DTT and Mg^{2+} (/), with only Mg^{2+} (Mg), or with both DTT and
622 Mg^{2+} (DTT + Mg). Specific activities are reported as µmol(NADPH) min^{-1} mg(SBPase)$^{-1}$.
623
624 **Supplementary movie 1. Molecular dynamics simulation of *Cr*SBPase 7B2O chain A upon C115-120**
625 **disulfide bridge reduction.**
626
627 **Supplementary movie 2. Molecular dynamics simulation of *Cr*SBPase 7B2O chain B upon C115-120**
628 **bridge reduction.**
629
630

Authors contributions

JH, NC: Conceptualization; JH, NC, MS, TLM: Data curation; JH, NC, MZ: Formal analysis; JH: Funding acquisition; JH, NC, MZ, SDL, MS, TLM: Investigation; JH, NC, MZ, MS, TLM: Methodology; JH, SDL: Project administration; JH, NC, SDL: Resources; NC: Software; JH, MZ: Supervision; JH, NC, MZ, SDL, MS, TLM: Writing - original draft; JH, NC, MZ, SDL, MS, TLM: Writing - review & editing.

Acknowledgements

We acknowledge the Institut de Biologie Physico-Chimique (CNRS, FR 505) for access to the crystallization facility. We acknowledge SOLEIL for provision of synchrotron radiation facilities at beamlines SWING, PROXIMA-1, and PROXIMA-2A. We thank Guillaume Q. Robert for his contribution to protein purification, crystallization under reducing treatment, and model building. Plasmids pSL-175, -181, and -182 were cloned by Dr. Laure Michelet. This work was funded by the grant CALVINTERACT from the Agence Nationale de la Recherche (ANR-19-CE11-0009). Martina Santoni received funding from the University of Bologna (Bologna, Italy) and Sorbonne University (Paris, France) exchange program ERASMUS+. This work was performed using HPC resources from GENCI–IDRIS (Grant 2021-077156). The authors express their gratitude to the financial support of the AAP AIN INSB CNRS.

Conflicts of interest statement

The authors report no conflict of interest relevant to the conduct or report of this research.

Bibliography

Abramson, J., J. Adler, J. Dunger, R. Evans, T. Green, A. Pritzel, O. Ronneberger, L. Willmore, A. J. Ballard, J. Bambrick, S. W. Bodenstein, D. A. Evans, C.-C. Hung, M. O'Neill, D. Reiman, K. Tunyasuvunakool, Z. Wu, A. Žemgulytė, E. Arvaniti, C. Beattie, O. Bertolli, A. Bridgland, A. Cherepanov, M. Congreve, A. I. Cowen-Rivers, A. Cowie, M. Figurnov, F. B. Fuchs, H. Gladman, R. Jain, Y. A. Khan, C. M. R. Low, K. Perlin, A. Potapenko, P. Savy, S. Singh, A. Stecula, A. Thillaisundaram, C. Tong, S. Yakneen, E. D. Zhong, M. Zielinski, A. Žídek, V. Bapst, P. Kohli, M. Jaderberg, D. Hassabis and J. M. Jumper (2024). "Accurate structure prediction of biomolecular interactions with AlphaFold 3." Nature.

Adams, P. D., P. V. Afonine, G. Bunkóczi, V. B. Chen, N. Echols, J. J. Headd, L. W. Hung, S. Jain, G. J. Kapral, R. W. Grosse Kunstleve, A. J. McCoy, N. W. Moriarty, R. D. Oeffner, R. J. Read, D. C. Richardson, J. S. Richardson, T. C. Terwilliger and P. H. Zwart (2011). "The Phenix software for automated determination of macromolecular structures." Methods **55**(1): 94-106.

Ahmad, S., M. Gromiha, H. Fawareh and A. Sarai (2004). "ASAView: database and tool for solvent accessibility representation in proteins." BMC Bioinformatics **5**: 51.

Almagro Armenteros, J. J., M. Salvatore, O. Emanuelsson, O. Winther, G. von Heijne, A. Elofsson and H. Nielsen (2019). "Detecting sequence signals in targeting peptides using deep learning." Life Sci Alliance **2**(5).

Anderson, L. E. (1974). "Activation of pea leaf chloroplast sedoheptulose 1,7-diphosphate phosphatase by light and dithiothreitol." Biochem Biophys Res Commun **59**(3): 907-913.

Barciszewski, J., J. Wisniewski, R. Kolodziejczyk, M. Jaskolski, D. Rakus and A. Dzugaj (2016). "T-to-R switch of muscle fructose-1,6-bisphosphatase involves fundamental changes of secondary and quaternary structure." Acta Crystallogr D Struct Biol **72**(Pt 4): 536-550.

Cadet, F. and J. C. Meunier (1988). "pH and kinetic studies of chloroplast sedoheptulose-1,7-bisphosphatase from spinach (Spinacia oleracea)." Biochem J **253**(1): 249-254.

Calvin, M. (1962). "The path of carbon in photosynthesis." Science **135**(3507): 879-889.

Chiadmi, M., A. Navaza, M. Miginiac-Maslow, J. P. Jacquot and J. Cherfils (1999). "Redox signalling in the chloroplast: structure of oxidized pea fructose-1,6-bisphosphate phosphatase." EMBO J **18**(23): 6809-6815.

Cotton, C. A., B. V. Kabasakal, N. A. Miah and J. W. Murray (2015). "Structure of the dual-function fructose-1,6/sedoheptulose-1,7-bisphosphatase from Thermosynechococcus elongatus bound with sedoheptulose-7-phosphate." Acta Crystallogr F Struct Biol Commun **71**(Pt 10): 1341-1345.

Emanuelsson, O., S. Brunak, G. von Heijne and H. Nielsen (2007). "Locating proteins in the cell using TargetP, SignalP and related tools." Nat Protoc **2**(4): 953-971.

Emsley, P., B. Lohkamp, W. G. Scott and K. Cowtan (2010). "Features and development of Coot." Acta Crystallogr D Biol Crystallogr **66**(Pt 4): 486-501.

Feng, L., Y. Han, G. Liu, B. An, J. Yang, G. Yang, Y. Li and Y. Zhu (2007). "Overexpression of sedoheptulose-1,7-bisphosphatase enhances photosynthesis and growth under salt stress in transgenic rice plants." Funct Plant Biol **34**(9): 822-834.

Feng, L., K. Wang, Y. Li, Y. Tan, J. Kong, H. Li, Y. Li and Y. Zhu (2007). "Overexpression of SBPase enhances photosynthesis against high temperature stress in transgenic rice plants." Plant Cell Rep **26**(9): 1635-1646.

Franke, D., M. V. Petoukhov, P. V. Konarev, A. Panjkovich, A. Tuukkanen, H. D. T. Mertens, A. G. Kikhney, N. R. Hajizadeh, J. M. Franklin, C. M. Jeffries and D. I. Svergun (2017). "ATSAS 2.8: a comprehensive data analysis suite for small-angle scattering from macromolecular solutions." J Appl Crystallogr **50**(Pt 4): 1212-1225.

Giudici-Orticoni, M. T., J. Buc, M. Bidaud and J. Ricard (1990). "Thermodynamics of information transfer between subunits in oligomeric enzymes and kinetic cooperativity. 3. Information transfer between the subunits of chloroplast fructose bisphosphatase." Eur J Biochem **194**(2): 483-490.

Glaser, F., T. Pupko, I. Paz, R. E. Bell, D. Bechor-Shental, E. Martz and N. Ben-Tal (2003). "ConSurf: identification of functional regions in proteins by surface-mapping of phylogenetic information." Bioinformatics **19**(1): 163-164.

Gutle, D. D., T. Roret, S. J. Muller, J. Couturier, S. D. Lemaire, A. Hecker, T. Dhalleine, B. B. Buchanan, R. Reski, O. Einsle and J. P. Jacquot (2016). "Chloroplast FBPase and SBPase are thioredoxin-linked enzymes with similar architecture but different evolutionary histories." Proc Natl Acad Sci U S A **113**(24): 6779-6784.

Gütle, D. D., T. Roret, S. J. Müller, J. Couturier, S. D. Lemaire, A. Hecker, T. Dhalleine, B. B. Buchanan, R. Reski, O. Einsle and J. P. Jacquot (2016). "Chloroplast FBPase and SBPase are thioredoxin-linked enzymes with similar architecture but different evolutionary histories." Proc Natl Acad Sci U S A **113**(24): 6779-6784.

Hammel, A., F. Sommer, D. Zimmer, M. Stitt, T. Mühlhaus and M. Schroda (2020). "Overexpression of Sedoheptulose-1,7-Bisphosphatase Enhances Photosynthesis in Chlamydomonas reinhardtii and Has No Effect on the Abundance of Other Calvin-Benson Cycle Enzymes." Front Plant Sci **11**: 868.

Jacquot, J. P., J. Lopez-Jaramillo, M. Miginiac-Maslow, S. Lemaire, J. Cherfils, A. Chueca and J. Lopez-Gorge (1997). "Cysteine-153 is required for redox regulation of pea chloroplast fructose-1,6-bisphosphatase." FEBS Lett **401**(2-3): 143-147.

Johnson, M. P. (2016). "Photosynthesis." Essays Biochem **60**(3): 255-273.

Johnson, X. and J. Alric (2013). "Central carbon metabolism and electron transport in Chlamydomonas reinhardtii: metabolic constraints for carbon partitioning between oil and starch." Eukaryot Cell **12**(6): 776-793.

Jumper, J., R. Evans, A. Pritzel, T. Green, M. Figurnov, O. Ronneberger, K. Tunyasuvunakool, R. Bates, A. Zidek, A. Potapenko, A. Bridgland, C. Meyer, S. A. A. Kohl, A. J. Ballard, A. Cowie, B. Romera-Paredes, S. Nikolov, R. Jain, J. Adler, T. Back, S. Petersen, D. Reiman, E. Clancy, M. Zielinski, M. Steinegger, M. Pacholska, T. Berghammer, S. Bodenstein, D. Silver, O. Vinyals, A. W. Senior, K. Kavukcuoglu, P. Kohli and D. Hassabis (2021). "Highly accurate protein structure prediction with AlphaFold." Nature **596**(7873): 583-589.

Krissinel, E. and K. Henrick (2007). "Inference of macromolecular assemblies from crystalline state." J Mol Biol **372**(3): 774-797.

Kubis, A. and A. Bar-Even (2019). "Synthetic biology approaches for improving photosynthesis." J Exp Bot **70**(5): 1425-1433.

Lee, S. W. and T. R. Hahn (2003). "Light-regulated differential expression of pea chloroplast and cytosolic fructose-1,6-bisphosphatases." Plant Cell Rep **21**(6): 611-618.

Lefebvre, S., T. Lawson, O. V. Zakhleniuk, J. C. Lloyd, C. A. Raines and M. Fryer (2005). "Increased sedoheptulose-1,7-bisphosphatase activity in transgenic tobacco plants stimulates photosynthesis and growth from an early stage in development." Plant Physiol **138**(1): 451-460.

Lemaire, S. D., B. Guillon, P. Le Maréchal, E. Keryer, M. Miginiac-Maslow and P. Decottignies (2004). "New thioredoxin targets in the unicellular photosynthetic eukaryote *Chlamydomonas reinhardtii*." Proc Natl Acad Sci U S A **101**(19): 7475-7480.

Lemaire, S. D., D. Tedesco, P. Crozet, L. Michelet, S. Fermani, M. Zaffagnini and J. Henri (2018). "Crystal Structure of Chloroplastic Thioredoxin f2 from Chlamydomonas reinhardtii Reveals Distinct Surface Properties." Antioxidants (Basel) **7**(12).

Liebschner, D., P. V. Afonine, M. L. Baker, G. Bunkóczi, V. B. Chen, T. I. Croll, B. Hintze, L. W. Hung, S. Jain, A. J. McCoy, N. W. Moriarty, R. D. Oeffner, B. K. Poon, M. G. Prisant, R. J. Read, J. S. Richardson, D. C. Richardson, M. D. Sammito, O. V. Sobolev, D. H. Stockwell, T. C. Terwilliger, A. G. Urzhumtsev, L. L. Videau, C. J. Williams and P. D. Adams (2019). "Macromolecular structure determination using X-rays, neutrons and electrons: recent developments in Phenix." Acta Crystallogr D Struct Biol **75**(Pt 10): 861-877.

McConnell, E. W., E. G. Werth and L. M. Hicks (2018). "The phosphorylated redox proteome of Chlamydomonas reinhardtii: Revealing novel means for regulation of protein structure and function." Redox Biol **17**: 35-46.

753 Meloni, M., S. Fanti, D. Tedesco, L. Gurrieri, P. Trost, S. Fermani, S. D. Lemaire, M. Zaffagnini and J.
754 Henri (2024). "Characterization of chloroplast ribulose-5-phosphate-3-epimerase from the microalga
755 Chlamydomonas reinhardtii." Plant Physiol **194**(4): 2263-2277.
756 Mettler, T., T. Muhlhaus, D. Hemme, M. A. Schottler, J. Rupprecht, A. Idoine, D. Veyel, S. K. Pal, L.
757 Yaneva-Roder, F. V. Winck, F. Sommer, D. Vosloh, B. Seiwert, A. Erban, A. Burgos, S. Arvidsson, S.
758 Schonfelder, A. Arnold, M. Gunther, U. Krause, M. Lohse, J. Kopka, Z. Nikoloski, B. Mueller-Roeber, L.
759 Willmitzer, R. Bock, M. Schroda and M. Stitt (2014). "Systems Analysis of the Response of
760 Photosynthesis, Metabolism, and Growth to an Increase in Irradiance in the Photosynthetic Model
761 Organism Chlamydomonas reinhardtii." Plant Cell **26**(6): 2310-2350.
762 Moorhead, G. B., R. J. Hodgson and W. C. Plaxton (1994). "Copurification of cytosolic fructose-1,6-
763 bisphosphatase and cytosolic aldolase from endosperm of germinating castor oil seeds." Arch
764 Biochem Biophys **312**(2): 326-335.
765 Morisse, S., M. Zaffagnini, X. H. Gao, S. D. Lemaire and C. H. Marchand (2014). "Insight into protein S-
766 nitrosylation in Chlamydomonas reinhardtii." Antioxid Redox Signal **21**(9): 1271-1284.
767 Nishizawa, A. N. and B. B. Buchanan (1981). "Enzyme regulation in C4 photosynthesis. Purification
768 and properties of thioredoxin-linked fructose bisphosphatase and sedoheptulose bisphosphatase
769 from corn leaves." J Biol Chem **256**(12): 6119-6126.
770 Ohta, J. (2022). "A novel variant of the Calvin-Benson cycle bypassing fructose bisphosphate." Sci Rep
771 **12**(1): 3984.
772 Pérez-Pérez, M. E., A. Mauriès, A. Maes, N. J. Tourasse, M. Hamon, S. D. Lemaire and C. H. Marchand
773 (2017). "The Deep Thioredoxome in Chlamydomonas reinhardtii: New Insights into Redox
774 Regulation." Mol Plant **10**(8): 1107-1125.
775 Raines, C. A. (2022). "Improving plant productivity by re-tuning the regeneration of RuBP in the
776 Calvin-Benson-Bassham cycle." New Phytol **236**(2): 350-356.
777 Robert, X. and P. Gouet (2014). "Deciphering key features in protein structures with the new
778 ENDscript server." Nucleic Acids Research **42**(W1): W320-W324.
779 Rosenthal, D. M., A. M. Locke, M. Khozaei, C. A. Raines, S. P. Long and D. R. Ort (2011). "Over-
780 expressing the C(3) photosynthesis cycle enzyme Sedoheptulose-1-7 Bisphosphatase improves
781 photosynthetic carbon gain and yield under fully open air CO(2) fumigation (FACE)." BMC Plant Biol
782 **11**: 123.
783 Schmollinger, S., T. Mühlhaus, N. R. Boyle, I. K. Blaby, D. Casero, T. Mettler, J. L. Moseley, J. Kropat, F.
784 Sommer, D. Strenkert, D. Hemme, M. Pellegrini, A. R. Grossman, M. Stitt, M. Schroda and S. S.
785 Merchant (2014). "Nitrogen-Sparing Mechanisms in Chlamydomonas Affect the Transcriptome, the
786 Proteome, and Photosynthetic Metabolism." Plant Cell **26**(4): 1410-1435.
787 Schürmann, P. and B. B. Buchanan (1975). "Role of ferredoxin in the activation of sedoheptulose
788 diphosphatase in isolated chloroplasts." Biochim Biophys Acta **376**(1): 189-192.
789 Seuter, A., M. Busch and R. Hain (2002). "Overexpression of the potential herbicide target
790 sedoheptulose-1,7-bisphosphatase from Spinacia oleracea in transgenic tobacco." Molecular
791 Breeding **9**(1): 53-61.
792 Simkin, A. J., P. E. Lopez-Calcagno, P. A. Davey, L. R. Headland, T. Lawson, S. Timm, H. Bauwe and C.
793 A. Raines (2017). "Simultaneous stimulation of sedoheptulose 1,7-bisphosphatase, fructose 1,6-
794 bisphophate aldolase and the photorespiratory glycine decarboxylase-H protein increases CO(2)
795 assimilation, vegetative biomass and seed yield in Arabidopsis." Plant Biotechnol J **15**(7): 805-816.
796 Tamoi, M., M. Nagaoka and S. Shigeoka (2005). "Immunological properties of sedoheptulose-1,7-
797 bisphosphatase from Chlamydomonas sp. W80." Biosci Biotechnol Biochem **69**(4): 848-851.
798 Wagner, V., G. Gessner, I. Heiland, M. Kaminski, S. Hawat, K. Scheffler and M. Mittag (2006).
799 "Analysis of the phosphoproteome of Chlamydomonas reinhardtii provides new insights into various
800 cellular pathways." Eukaryot Cell **5**(3): 457-468.
801 Wang, L., W. Patena, K. A. Van Baalen, Y. Xie, E. R. Singer, S. Gavrilenko, M. Warren-Williams, L. Han,
802 H. R. Harrigan, V. Chen, V. T. N. P. Ton, S. Kyin, H. H. Shwe, M. H. Cahn, A. T. Wilson, J. Hu, D. J.
803 Schnell, C. D. McWhite and M. Jonikas (2022). "A Chloroplast Protein Atlas Reveals Novel Structures
804 and Spatial Organization of Biosynthetic Pathways." bioRxiv: 2022.2005.2031.493820.

805 Werth, E. G., E. W. McConnell, T. S. Gilbert, I. Couso Lianez, C. A. Perez, C. K. Manley, L. M. Graves, J.
806 G. Umen and L. M. Hicks (2017). "Probing the global kinome and phosphoproteome in
807 Chlamydomonas reinhardtii via sequential enrichment and quantitative proteomics." Plant J **89**(2):
808 416-426.
809 Woodrow, I. E. (1982). "Sedoheptulose-1,7-bisphosphatase from wheat chloroplasts." Methods
810 Enzymol **90 Pt E**: 392-396.
811 Woodrow, I. E. and D. A. Walker (1980). "Light-mediated activation of stromal sedoheptulose
812 bisphosphatase." Biochem J **191**(3): 845-849.
813 Yoshida, K. and T. Hisabori (2018). "Determining the Rate-Limiting Step for Light-Responsive Redox
814 Regulation in Chloroplasts." Antioxidants (Basel) **7**(11).
815 Zaffagnini, M., M. Bedhomme, C. H. Marchand, S. Morisse, P. Trost and S. D. Lemaire (2012). "Redox
816 regulation in photosynthetic organisms: focus on glutathionylation." Antioxid Redox Signal **16**(6):
817 567-586.
818 Zimmer, D., C. Swart, A. Graf, S. Arrivault, M. Tillich, S. Proost, Z. Nikoloski, M. Stitt, R. Bock, T.
819 Mühlhaus and A. Boulouis (2021). "Topology of the redox network during induction of
820 photosynthesis as revealed by time-resolved proteomics in tobacco." Sci Adv **7**(51): eabi8307.
821

Figure 1.

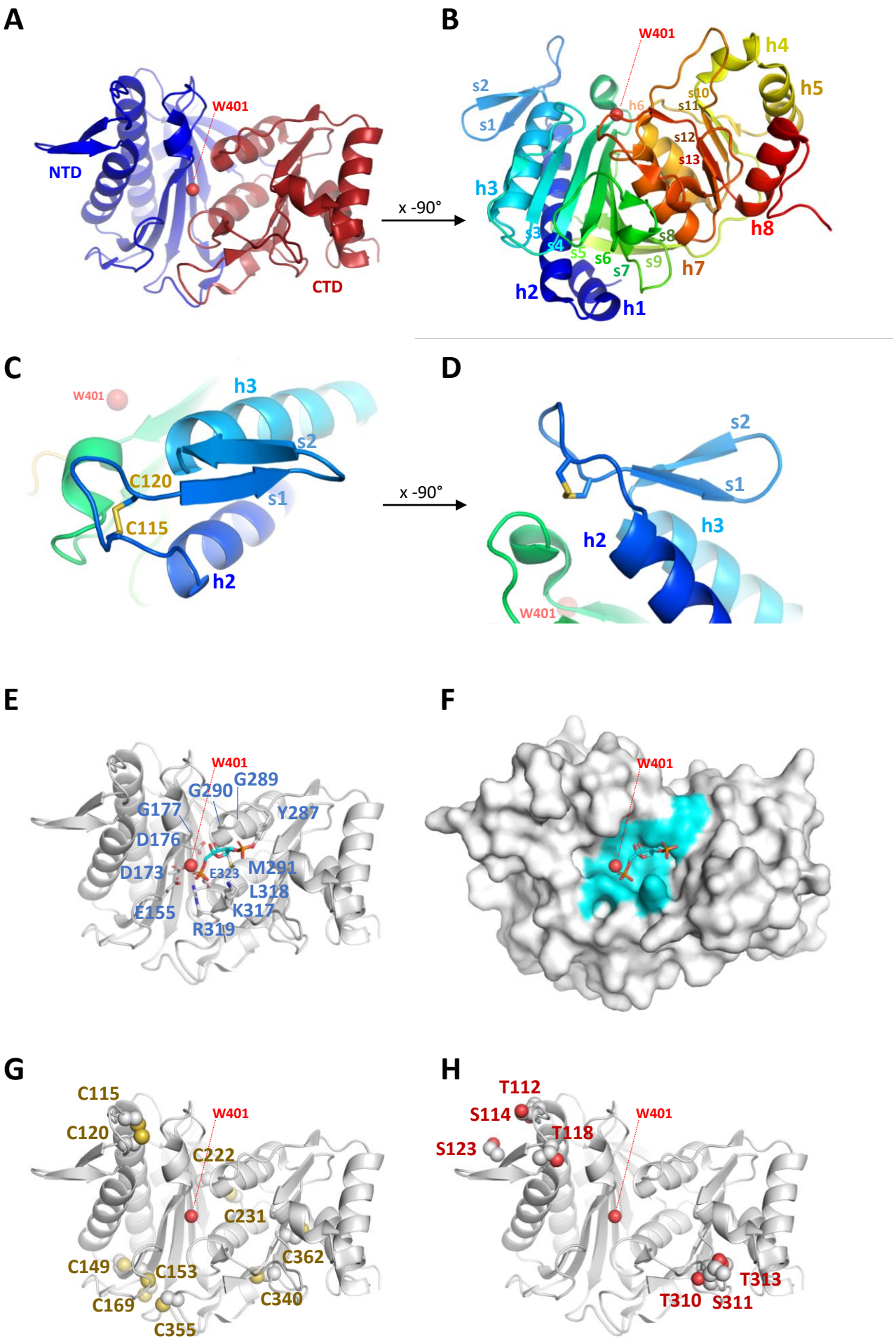
A
W401
NTD
CTD
x -90°
B
W401
h4
h5
s2
s1
h6
s10
s11
s12
s13
h3
s3
s4
s5
s6
s7
s8
s9
h7
h8
h2
h1
C
W401
h3
s2
C120
s1
C115
h2
x -90°
D
s2
s1
h3
h2
W401
E
W401
G289
G290
G177
Y287
D176
D173
E323
M291
L318
E155
K317
R319
F
W401
G
C115
C120
W401
C222
C231
C149
C153
C362
C169
C340
C355
H
T112
S114
W401
T118
S123
T313
T310
S311

Figure 2.

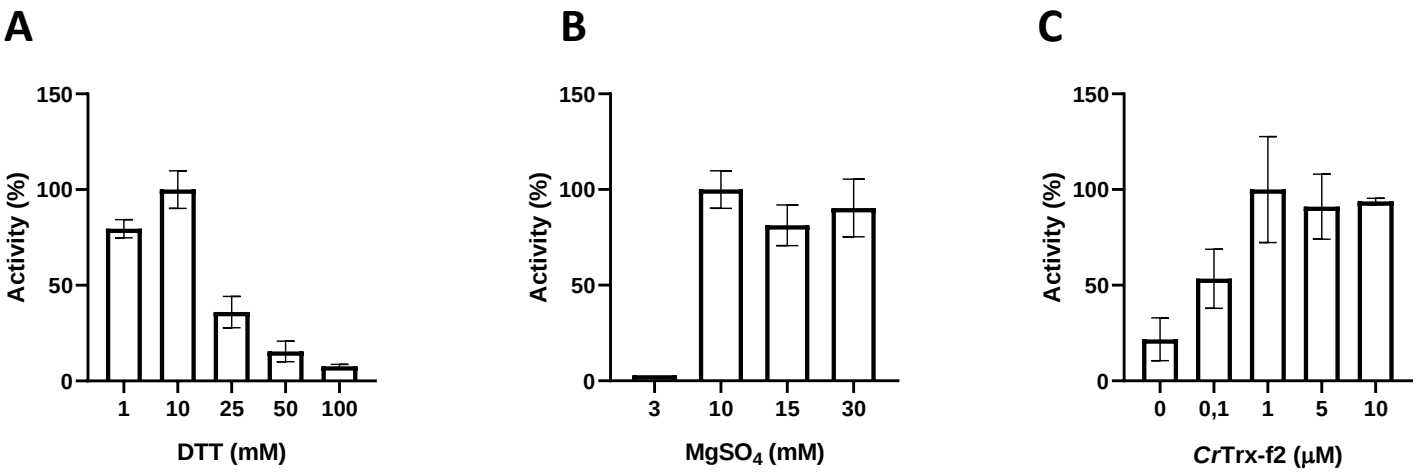
A
B
C
150
100
50
0
Activity (%)
1
10
25
50
100
DTT (mM)
3
10
15
30
MgSO4 (mM)
0
0,1
1
5
10
CrTrx-f2 (µM)

Figure 3.

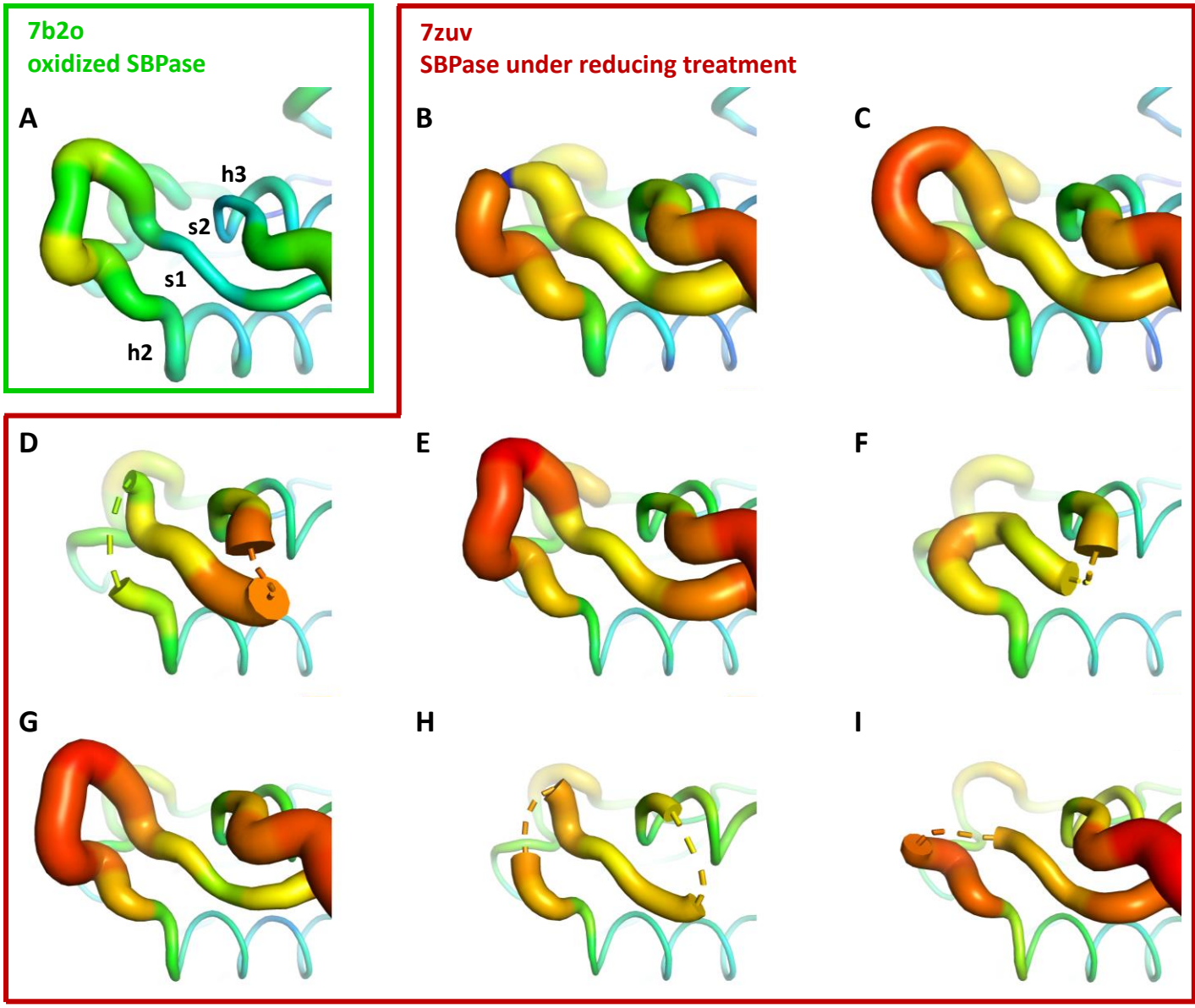
7b2o
oxidized SBPase
A
h3
s2
s1
h2
7zuv
SBPase under reducing treatment
B
C
D
E
F
G
H
I

Figure 4.

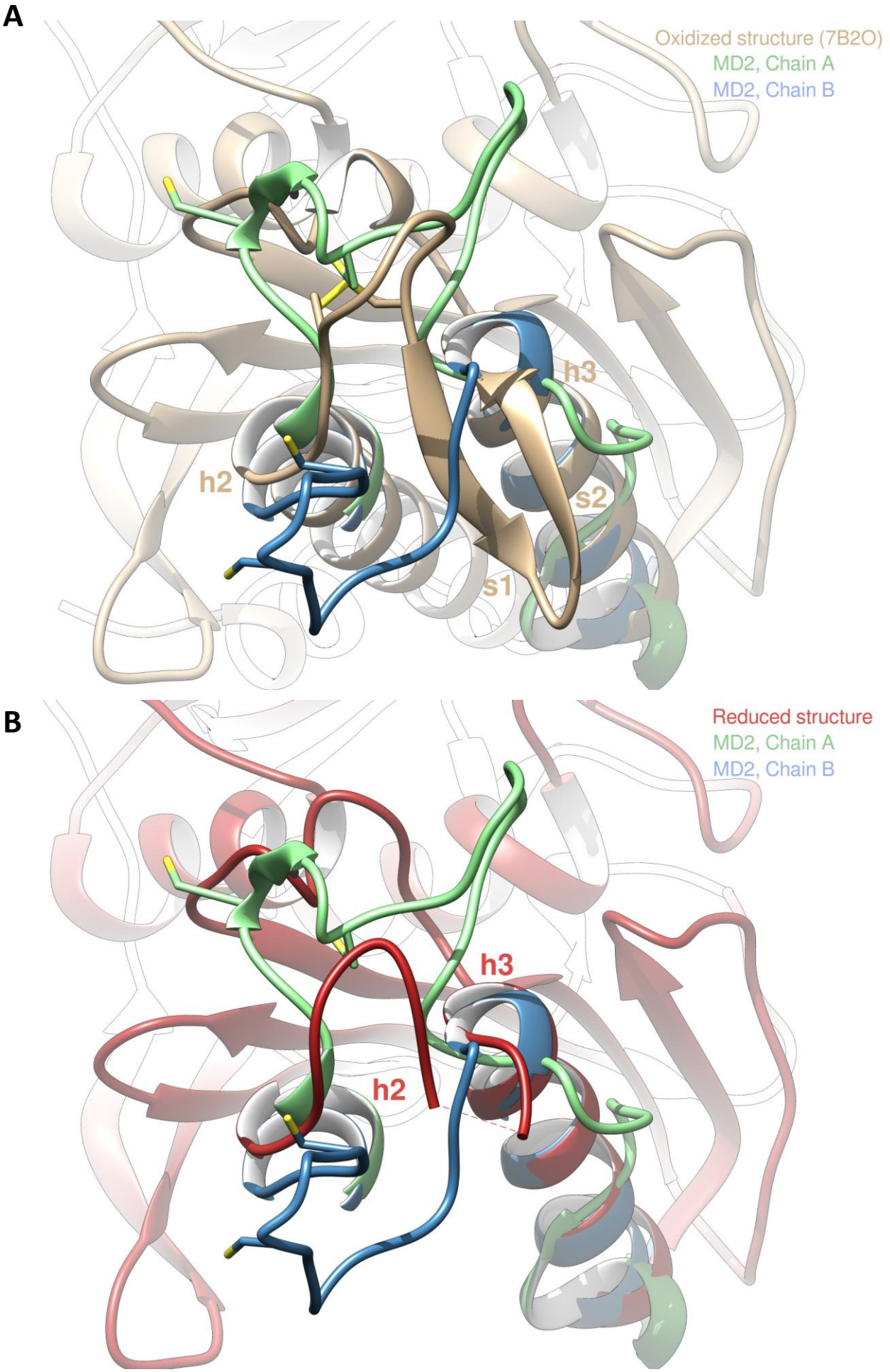
A
Oxidized structure (7B2O)
MD2, Chain A
MD2, Chain B
h3
h2
s2
s1
B
Reduced structure
MD2, Chain A
MD2, Chain B
h3
h2

Figure 5.

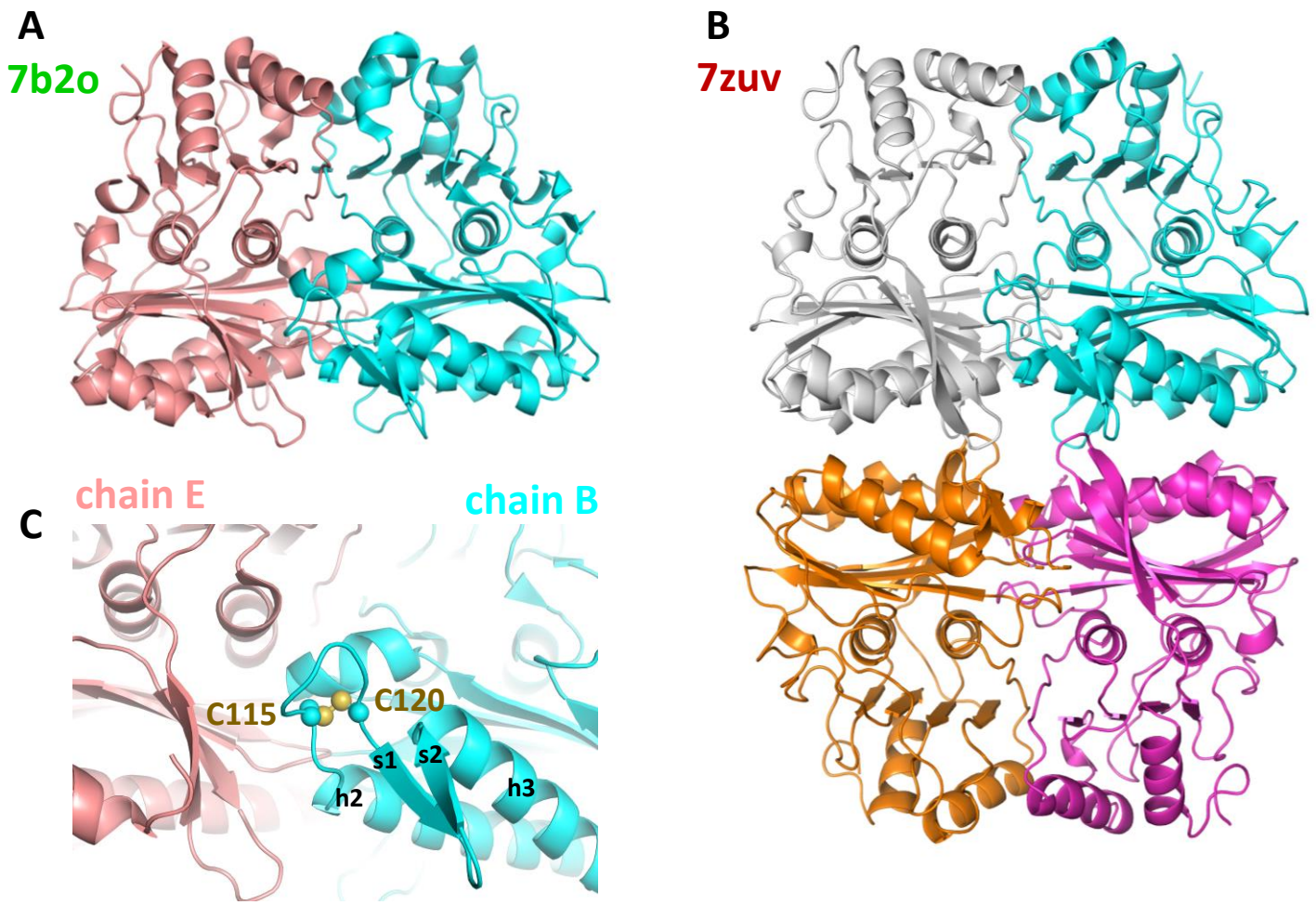

Figure 6.

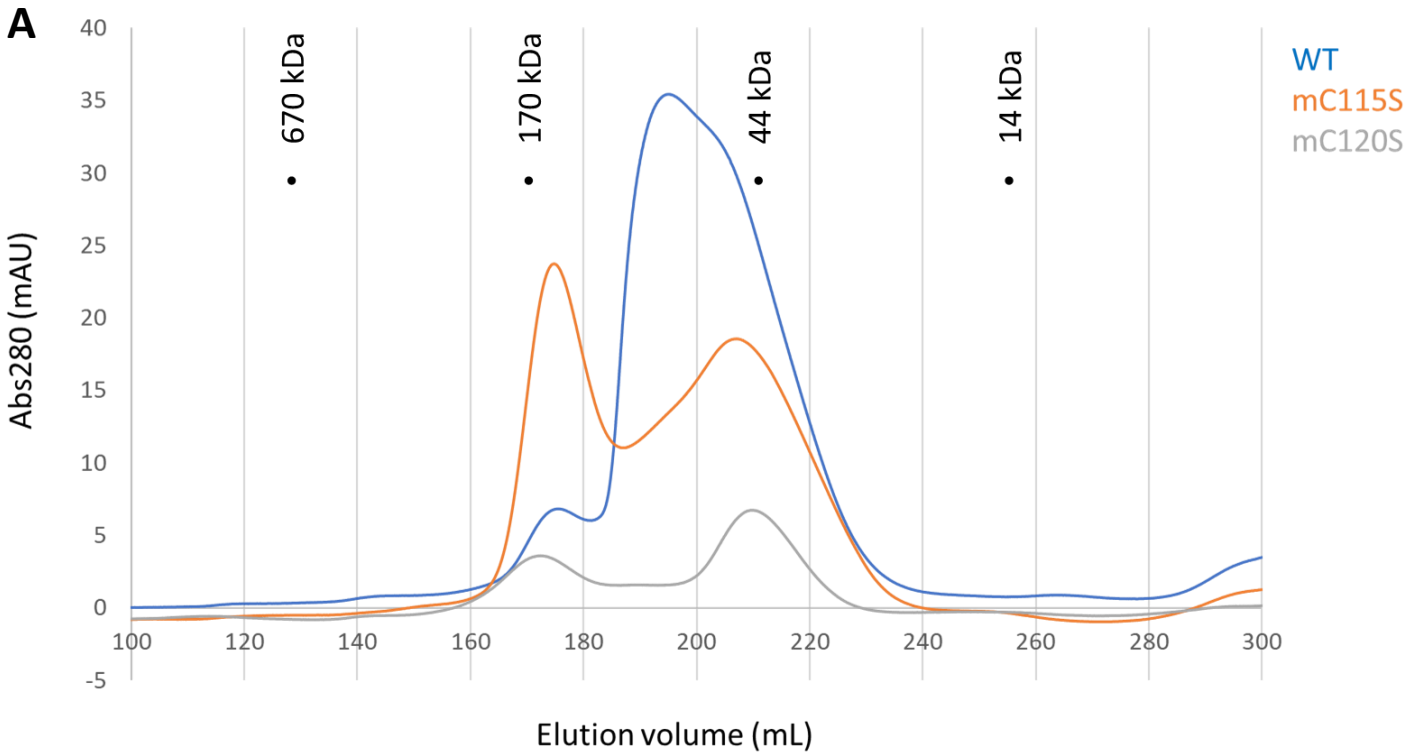
A
670 kDa
170 kDa
44 kDa
14 kDa
WT
mC115S
mC120S
Abs280 (mAU)
Elution volume (mL)

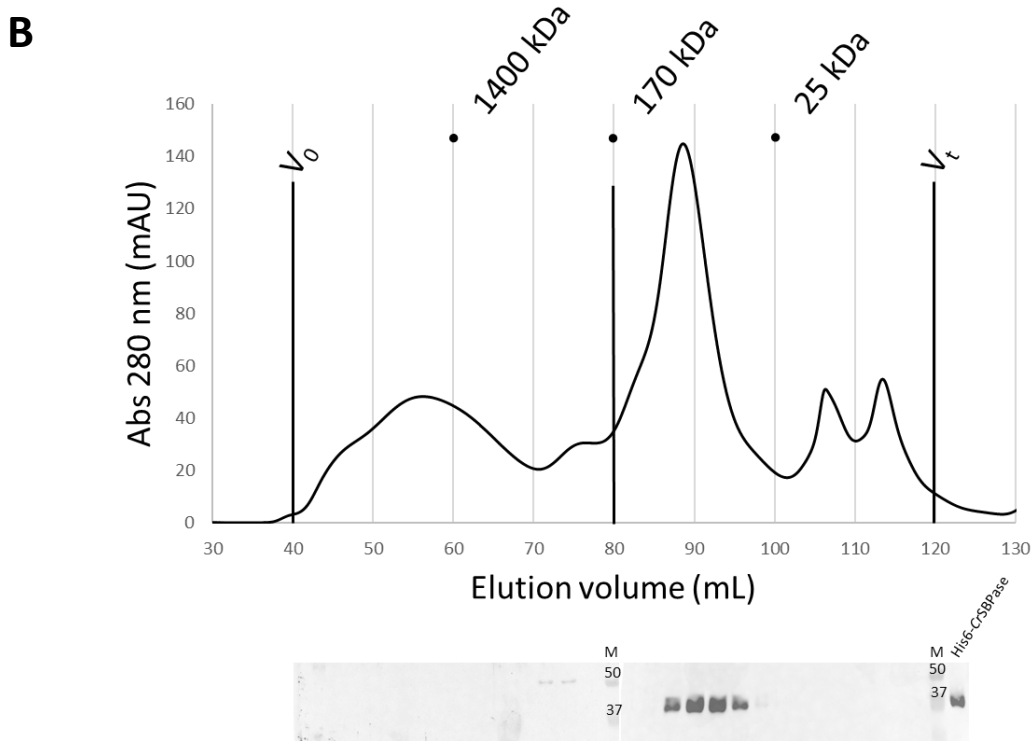
B
1400 kDa
170 kDa
25 kDa
V_o
V_t
Abs 280 nm (mAU)
Elution volume (mL)
M
50
37
M
50
37
His6-CrSBPase